Exploring the Emission Mechanisms of Mrk 180 with Long-term X-Ray and γ-Ray Data

Sandeep Kumar Mondal[1] , Saikat Das[2] , and Nayantara Gupta[1]

[1] Astronomy & Astrophysics Group, Raman Research Institute, C.V. Raman Avenue, Sadashivanagar, Bangalore 560080, Karnataka, India; skmondal@rri.res.in, nayan@rri.res.in

[2] Yukawa Institute for Theoretical Physics, Kyoto University, Kitashirakawa Oiwakecho, Sakyo-ku, Kyoto 606-8502, Japan; saikat.das@yukawa.kyoto-u.ac.jp

Abstract

Markarian (Mrk) 180 is a BL Lacertae object located at a redshift of 0.045 and is a potential candidate for high-energy cosmic-ray acceleration. We have analyzed the Fermi Large Area Telescope (Fermi-LAT) γ-ray data of Mrk 180 collected over a period of 12.8 yr and found no significant enhancement in the flux from the long-term γ-ray light curve. We have also analyzed Swift X-ray, ultraviolet, and optical, and X-ray Multi-Mirror Mission (XMM-Newton) data to construct the multiwavelength spectral energy distribution (SED). The SED has been modeled with one-zone pure leptonic and lepto-hadronic scenarios to explain the underlying physics of multiwavelength emission. The pure leptonic model and the two lepto-hadronic models, viz., (i) line-of-sight interactions of ultrahigh-energy cosmic rays (UHECRs; $E \gtrsim 10^{17}$ eV) with the cosmic background radiation and (ii) the interactions of relativistic protons with the cold protons in the jet, have been compared in our work. Moreover, an earlier study has associated Mrk 180 with the Telescope Array (TA) hotspot of UHECRs at $E > 57$ EeV. This speculation motivates us to check whether ultrahigh-energy protons and iron nuclei can reach the Earth from Mrk 180. After comparing the results of our simulation with the current observational data, we find that Mrk 180 is unlikely to be a source of the UHECR events contributing to the TA hotspot for conservative strengths of extragalactic magnetic fields.

Unified Astronomy Thesaurus concepts: High energy astrophysics (739); Gamma-ray astronomy (628); Active galactic nuclei (16); Blazars (164); Cosmic ray sources (328)

1. Introduction

The central emission core of active galaxies is powered by accretion onto a supermassive black hole (SMBH). This leads to the formation of a collimated jet of outflow, along the angular momentum direction, that outshines the entire galaxy (Urry & Padovani 1995). Active galactic nuclei (AGNs) are some of the most prominent sources of high-energy γ-rays. The jet transports energy and momentum over large distances. In the case of blazars, the jet points along the observer's line of sight and provides a unique testbed to study the acceleration of cosmic rays (see Blandford et al. 2019, for a recent review). Blazars show high flux variability; their emission is highly polarized and of nonthermal origin. They are broadly classified into flat-spectrum radio quasars (FSRQs) having broad emission lines, and BL Lac objects showing a featureless continuum spectrum.

The broadband SED of a blazar covers the entire electromagnetic spectrum, ranging from radio to very high-energy (VHE, $E \gtrsim 30$ GeV) γ-rays. It exhibits two peak emission frequencies. The low-energy peak occurs between radio and soft X-ray energies and can be attributed to synchrotron radiation from a relativistic electron and positron population. The high-energy peak between X-ray and VHE γ-ray energies can arise from various processes. The most prevalent explanation is the inverse Compton scattering of synchrotron photons (synchrotron self-Compton, SSC) or external photons originating from the broad-line region (BLR), the dusty torus (DT), or the accretion disk (AD). In addition, the VHE γ-rays can also come from photohadronic (pγ) or hadronuclear (pp) interactions of accelerated cosmic rays with the ambient radiation or matter in the emission region of the jet or proton synchrotron radiation (Tchernin et al. 2014; Blandford et al. 2019; Cerruti 2020).

Mrk 180 was discovered by Swiss-origin astronomer Fritz Zwicky and later identified as a BL Lac object in 1976 by spectral analysis. It is a high-synchrotron peaked BL Lac (HBL) object embedded at the center of an elliptical galaxy (Mufson & Hutter 1981), located at redshift $z = 0.0458$ (Ulrich 1978) with R.A. = 174°.11008, decl. = 70°.1575. This source was detected for the first time in X-rays by HEAO-1 (Hutter & Mufson 1981); since then it has been monitored by several telescopes, e.g., Fermi-LAT, Swift, Major Atmospheric Gamma Imaging Cherenkov Telescope (MAGIC), XMM-Newton, Monitoring Of Jets in Active galactic nuclei with VLBA Experiments (MOJAVE), Kungliga Vetenskapsakademien, Royal Swedish Academy of Sciences (KVA), and All-Sky Monitor (ASM). In 2006 March, VHE γ-ray emission was detected for the first time (Albert et al. 2006) from this source, triggered by an optical burst. Rügamer et al. (2011a, 2011b) carried out a multiwavelength study of this source. Mrk 180 was also monitored for a long period (2002–2012) in the optical wave band and its light curve was analyzed (Nilsson et al. 2018).

The Telescope Array (TA) experiment, located in Utah, United States, is a state-of-the-art detector observing ultrahigh-energy cosmic rays (UHECRs; $E \gtrsim 10^{17}$ eV) in the Northern Hemisphere. Based on an intermediate-scale anisotropy search using 5 yr of data, the TA collaboration had earlier reported a cluster of events at R.A. = 146°.7 and decl. = 43°.2, found by oversampling in circles of 20° radius (Abbasi et al. 2014). 72 UHECR events were detected in this direction at $E > 57$ EeV, where TA has 100% detection efficiency. The hotspot had a Li–Ma significance

of 5.1σ. He et al. (2016) identified Mrk 180 as a possible source of UHECRs in the context of explaining the origin of the TA hotspot (Abbasi et al. 2014; Kawata et al. 2015, 2019). Motivated by the earlier studies, we carry out a comprehensive study of Mrk 180 to ascertain the underlying mechanism of high-energy γ-ray emission and whether it can be the source of UHECRs beyond 57 EeV contributing to the TA hotspot.

We have analyzed the Fermi-LAT data collected over a period of 12.8 yr, the Swift XRT and UVOT data, and in addition to these the XMM-Newton X-ray data to construct the broadband SED of this source. Section 2 is dedicated to discussions of the methods followed to analyze the data. We have also searched for fluctuations in the γ-ray flux in the Fermi-LAT light curve, as discussed in Section 3. Subsequently, we build the long-term multiwavelength SED. We discuss the theoretical framework for SED modeling in Section 4. We present our results in Section 5 and discuss them in Section 6. Finally, we draw our conclusions in Section 7.

2. Data Analysis

2.1. Fermi-LAT Data Analysis

The Fermi-LAT is an imaging, pair-conversion, wide-field-of-view, high-energy γ-ray telescope that can detect photons of energy 20 MeV to more than 300 GeV, whose field of view is 2.4 sr (Atwood et al. 2009). Fermi carries two instruments: one is the LAT and the other is the Gamma-ray Burst Monitor (GBM). The LAT is Fermi's primary instrument. Fermi scans the whole sky every three hours. It was launched in 2008 June in a near-Earth orbit and still in operation. The Pass 8 Fermi-LAT γ-ray data of Mrk 180 were extracted from the Fermi Science Support Center (FSSC) data server (Fermi-LAT_Data_Server 2022) for a period of more than 12.8 yr (2008 August–2021 May). We have used Fermipy (v1.0.1; Wood et al. 2017), an open-source Python package to analyze Fermi-LAT γ-ray data. Moreover, we have used the Fermi-LAT Fourth Source Catalog Data Release 2 (4FGL-DR2; gll_psc_v27.fits; Ballet et al. 2020). We have modeled the Galactic diffuse emission by the latest model template (gll_iem_v07; Acero et al. 2016) and we have considered iso_P8R3_SOURCE_V2_v1.txt for the extragalactic isotropic diffuse emission model. We have followed Fermipy's documentation for further analysis (Fermipy Document 2022) and extracted the light curve and SED of Mrk 180.

The photon-like events are classified as evclass = 128. The Fermi-LAT collaboration recommended to use the "SOURCE" event class for relatively small regions of interest ($<25°$, Bruel et al. 2018) and we have used the "P8R3 SOURCE" event class for which "evclass" has to be set to a value of 128 (Fermi-LAT Ciceron 2022) and evtype = 3; each event class includes different event types, which allows us to select events based on different criteria. The standard value of "evtype" is 3, which includes all types of events, i.e., front and back sections of the tracker (denoted by FRONT+BACK), for a given class. We have extracted the Fermi-LAT γ-ray data from the FSSC data server considering a search radius of 30° around the source Mrk 180. During the data preparation, we have selected a "region of interest" (ROI) of 10°, as suggested in Fermi's Data Preparation page,[3] and the maximum zenith angle of 90° was chosen to avoid contamination from Earth's limb in our analysis. We
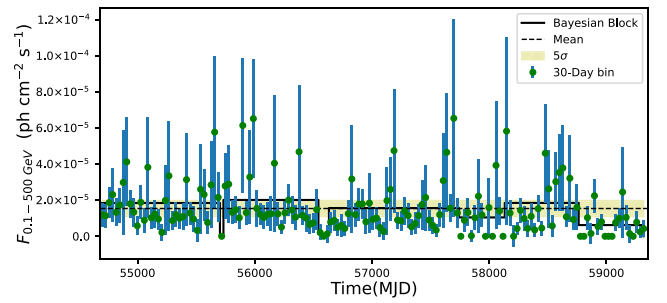

Figure 1. Application of the Bayesian block method to Fermi-LAT γ-ray data from Mrk 180 (MJD 54,682.65–59,355.67).

restricted our analysis to an energy range of 100 MeV to 500 GeV. We have obtained the γ-ray light curve shown in Figure 1 and the SED, which is used to construct the multiwavelength SED shown in Figures 2, 3, and 4.

2.2. Swift XRT and UVOT Data Analysis

The Neil Gehrels Swift observatory is a multiwavelength space-based observatory with three instruments on board: the Burst Alert Telescope (BAT; 15.0–150.0 keV), X-Ray Telescope (XRT; 0.3–10.0 keV), and Ultraviolet and Optical Telescope (UVOT; 170–600 nm) (Burrows et al. 2005). It observes the sky in the hard X-ray, soft X-ray, ultraviolet, and optical wave bands. Swift provides simultaneous data from any transient activity in all wave bands ranging from X-ray to optical. We collected all the XRT and UVOT data available for Mrk 180 over the period 2008 August to 2021 May. We have analyzed 44 observations. The standard data reduction procedure[4] has been followed to extract the source and background region.

In Swift XRT data, we have used clean event files corresponding to photon-count mode (PC mode), which we have obtained using the task "xrtpipeline" version 0.13.5. The calibration file (CALDB), version 20190910, and other standard screening criteria have been applied to the cleaned data. A radius of interest of 20–30 pixels has been considered to mark the source region; the radius of the background region is also the same, but it is far away from the source region. With the help of the "xselect" tool, we have selected the source region and background region and saved the spectrum files of the corresponding regions. Then "xrtmkarf" and "grppha" tools have been used to generate ancillary response files (arfs) and group the spectrum files with the corresponding response matrix file (rmf); then "addspec" and "mathpha" have been used. Thus we have obtained the spectrum. Thereafter, the spectrum has been modeled with xspec (v12.11.0; Arnaud 1996) tools. We have included the absorption by neutral hydrogen having column density,[5] $N_H = 1.37 \times 10^{20}$ cm^{-2} (HI4PI Collaboration et al. 2016). The final X-ray SED obtained in this way is shown in Figures 2, 3, and 4.

Mrk 180 was also monitored by Swift-UVOT in all six filters: U (3465 Å), V (5468 Å), B (4392 Å), UVW1 (2600 Å), UVM2 (2246 Å), and UVW2 (1928 Å). The source region has been extracted from a region of 5″ around the source, keeping the source at the center of the circle. The background region has been taken $\sim$3 times larger than the source region and it is far away from the source region. Using the "uvotsource" tool,
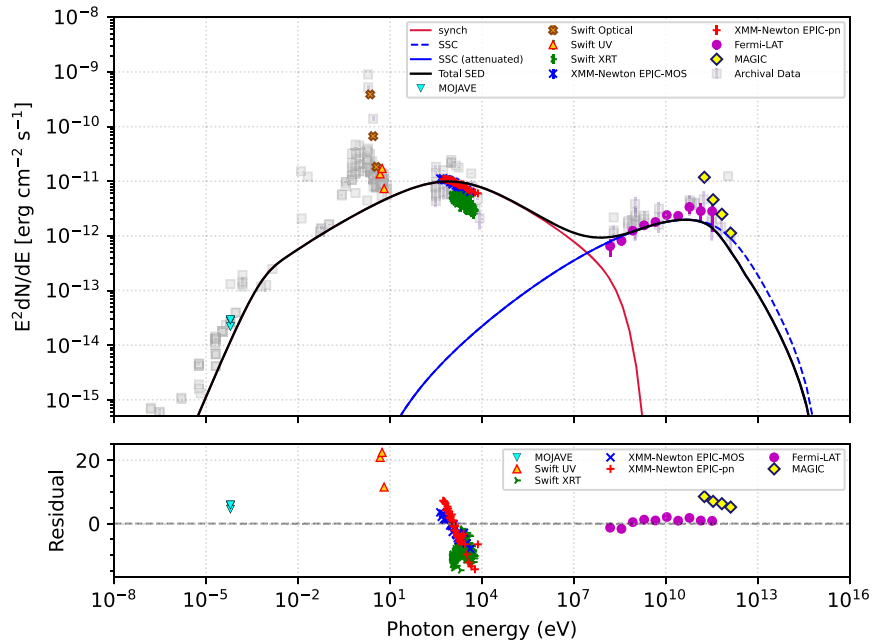

Figure 2. Pure leptonic modeling of the multiwavelength SED of Mrk 180 and residual plot corresponding to this modeling. The data color codes are mentioned in the plots.

we have extracted the source magnitude. This magnitude does not include the Galactic absorption, so it has been corrected. The Python module "extinction" (Extinction 2016) has been used to get the extinction values corresponding to all the Swift-UVOT filters. We have considered a Fitzpatrick (1999) dust extinction function for $R_V = 3.1$, where R_V is a dimensionless quantity that is the slope of the extinction curve. For diffuse interstellar medium (ISM) the mean value of R_V is 3.1 (Schultz & Wiemer 1975; Whittet & van Breda 1980; Rieke & Lebofsky 1985). Following are the values of the extinction coefficients of different Swift-UVOT wave bands that we have used in this work; U: 0.05584, V: 0.03460, B: 0.04603, UVW1: 0.07462, UVM2: 0.10383, UVW2: 0.09176.

2.3. XMM-Newton X-Ray Data Analysis

XMM-Newton is a space-borne X-ray observatory, consisting of three imaging X-ray cameras (European Photon Imaging Camera or EPIC), two grating X-ray spectrometers (reflection grating spectrometer or RGS), and one optical monitor (OM). It was launched on 1999 December 10. Because of its great capacity to detect X-rays, it was formerly known as the High Throughput X-ray Spectroscopy Mission. Now it is called XMM because of its multimirror design. The three EPICs are the primary instrument aboard XMM-Newton; of the three, two of them are MOS-CCD cameras and the remaining one is a pn-CCD camera. The energy range of the EPIC is about 0.15–15.0 keV. The MOS-CCD cameras are used to detect low-energy X-rays, whereas the pn-CCD camera is used to detect high-energy X-rays. The RGS operates from 0.35 to 2.1 keV. The OM covers from 170 to 650 nm. From the data archive of XMM-Newton,[6] we found two observations for Mrk 180: 0094170101 and 0094170301 of 20 ks and 8 ks respectively. We have followed the standard data reduction procedure[7] to extract the SED. We have extracted SED points

from MOS1 and MOS2, combined them, and finally obtained SED points from MOS. Also, we extracted SED points from the pn detector. Thereafter, we used xspec (v12.11.0; Arnaud 1996) to model these spectra. Apart from X-ray data, we have also analyzed OM image-mode data. We prepared the data following the same reduction procedure; then we used "omichain" for further analysis. We followed omichain (2018) instructions for the last step. By using the "om2pha" (om2pha 2016) command, we extracted the spectrum file to analyze in xspec. For this step, the required OM response files have been copied from OMResponseFile (2008). The first observation, 0094170101, contains single data corresponding to the u band, which is insufficient for further analysis, whereas the second observation, 0094170301, does not contain any image file for further study. So, our multiwavelength data do not contain any XMM-Newton OM data.

2.4. MOJAVE Data

MOJAVE is a long-term program to monitor radio brightness and polarization variation in jets associated with active galaxies visible in the northern sky (MOJAVE Webpage 2016). MOJAVE observes at three wavelengths—7 mm, 1.3 cm, and 2 cm; to obtain a full polarization image with an angular resolution better than 1 mas. We have collected MOJAVE data for Mrk 180 from the MOJAVE/2 cm Survey Data Archive (MOJAVE_Source_-Page 2016). There are seven observations in the archive and we used those data to construct the multiwavelength SED.

2.5. MAGIC Data

MAGIC is a system of two imaging atmospheric Cherenkov telescopes (IACTs), situated on the Canary Island of La Palma. VHE γ-rays impinging the Earth's upper atmosphere initiate cascade interactions, leading to the production of a shower of secondary particles, mainly electrons and positrons. Electrons and positrons moving faster than the phase velocity of light in the atmosphere emit Cherenkov radiation mainly in the UV–
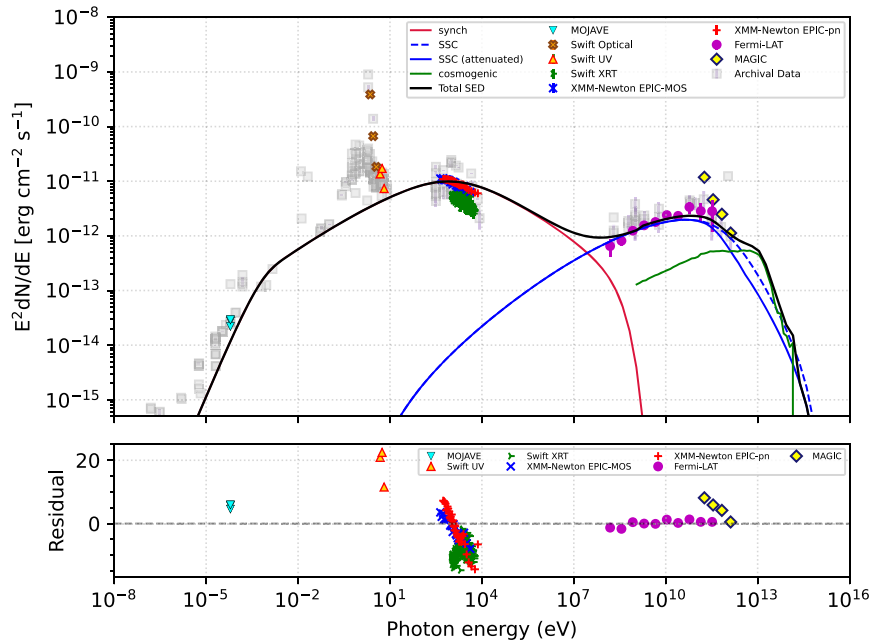

Figure 3. Leptonic+hadronic (UHECR) modeling of the multiwavelength SED of Mrk 180 and residual plot corresponding to this modeling.

blue band for a duration of a few nanoseconds. MAGIC collects the Cherenkov light and focuses it onto a pixelized camera, composed of 576 photomultipliers. Using dedicated image reconstruction algorithms, the energy and incoming direction of the primary γ-ray are calculated (Doro et al. 2008). This telescope can detect γ-rays of energy from 30 GeV to 100 TeV. VHE γ-rays from Mrk 180 were detected during an optical outburst in 2006 (Albert et al. 2006). We have used those data from MAGIC Data Centre (2006) for our study.

2.6. Archival Data

We have collected the archival data from Space Science Data Center SED builder (SSDC 2000) and shown them with gray squares in the multiwavelength SEDs (Figures 2, 3, and 4).

3. Analysis of the Fermi-LAT Gamma-Ray Light Curve

We analyzed 12.8 yr (MJD 54,682.65–59,355.67) of Fermi-LAT γ-ray data. Figure 1 is the 30 day binned Fermi-LAT γ-ray light curve. We have used the Bayesian block method (Scargle et al. 2013) to detect any fluctuations. We have not found any significant variation in the γ-ray flux. Though there are a few data points with high γ-ray flux, those points have large error bars, so further analysis with a smaller bin size is not feasible in this case. We proceed to build up the SED with the long-term data, as this source does not have any obvious temporal features.

4. Multiwavelength SED Modeling

Fermi-LAT γ-ray, Swift X-ray, ultraviolet, and optical data, and XMM-Newton X-ray data have been analyzed and archival data from MOJAVE, MAGIC, and SSDC have been compiled to plot the SED covering radio to VHE γ-ray frequencies. As discussed previously, Figures 2, 3, and 4 shows the double hump structure of the blazar SEDs. We have modeled the SED using pure leptonic and lepto-hadronic scenarios. For the latter, we consider the line-of-sight component of the electromagnetic cascade, initiated by UHECR interactions (Essey &

Kusenko 2010; Essey et al. 2010), and also pp interaction as the origin of VHE γ-rays. An external radiation field is required to produce a significant flux of secondary γ-rays in pγ interactions, hence we do not include this scenario in this work. In the following subsections, we discuss the models used in this work to explain the multiwavelength SED of Mrk 180.

4.1. Leptonic Modeling

We have considered a spherical emission region of radius R within the jet, moving with a Doppler factor δ_D, where relativistic electrons and positrons accelerated in the jet lose energy through synchrotron radiation in a steady and uniform magnetic field B, and also by SSC emission. From the maximum likelihood analysis of Fermi-LAT data, a log-parabolic injection was found to best fit the data. Massaro et al. (2004) showed that a log-parabolic photon spectrum can be produced from the radiative loss of a log-parabolic electron spectrum. So, we have used the log-parabolic spectrum of the injected electrons in the blob to explain the multiwavelength SED of Mrk 180, given by the following expression:

$$Q(E) = L_0(E/E_0)^{-(\alpha + \beta \log_{10}(E/E_0))}, \quad (1)$$

where $Q(E)$ is the log-parabolic distribution, L_0 is the normalization constant, E_0 is the scaling factor or pivot energy, which is set to 97 MeV in our modeling and kept fixed, α is the spectral index, and β is the curvature index.

We have used the open-source code GAMERA (2016; Hahn 2016) to model the multiwavelength leptonic emission. It solves the time-dependent transport equation and propagates the particle spectrum $N(E, t)$ for an injected spectrum $Q(E)$ to calculate the synchrotron and SSC emissions including the Klein–Nishina effect. GAMERA solves the following transport equation:

$$\frac{\partial N(E, t)}{\partial t} = Q(E) - \frac{\partial}{\partial E}(b(E, t)N(E, t)) - \frac{N(E, t)}{\tau_{esc}} \quad (2)$$

where $Q(E)$ is the input particle spectrum and $b(E, t)$ corresponds to the rate of energy loss by synchrotron and
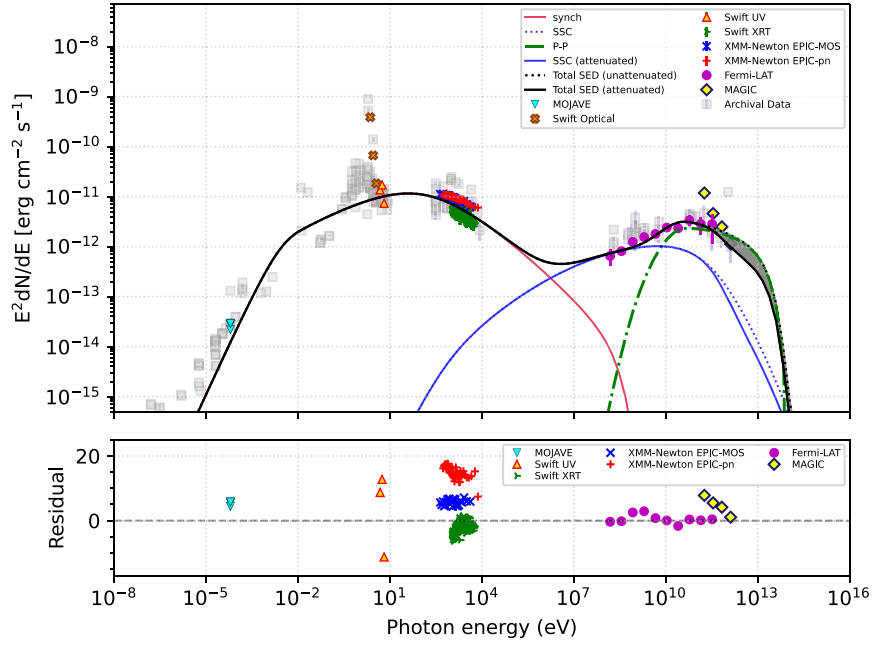
Figure 4. Leptonic+hadronic (pp) modeling of the multiwavelength SED of Mrk 180 and residual plot corresponding to this modeling; the gray shaded region denotes the difference between the attenuated and unattenuated regions of the total SED.

SSC emission. The term $\tau_{esc}(E, t)$ denotes the escape time of particles from the emission region. We consider a constant escape of the electrons from the emission region over the dynamical timescale $\tau_{esc} \sim R/c$, where c is the speed of light. We find that the time-evolved electron spectrum reaches a steady state after nearly 100 days, and this spectrum has been used in this work.

4.2. UHECR Interactions

We have assumed a power-law injection of the protons into the ISM of the following form:

$$N_p(E_p) = \frac{dN}{dE_p} = A_p E_p^{-\alpha_p} \qquad (3)$$

where A_p is the normalization constant of the injected proton spectrum and α_p is the spectral index, which is the same for electrons and protons because they are accelerated in the same region. We have taken the minimum energy of protons $E_{p,min} = 0.1$ EeV and the maximum energy of protons $E_{p,max} = 100$ EeV.

The ultrahigh-energy protons escape from the emission region and propagate through the extragalactic medium interacting with cosmic microwave background (CMB) and extragalactic background light (EBL) photons. In this process, electrons, positrons, γ-rays, and neutrinos are produced through Δ-resonance and Bethe–Heitler pair production. Protons interact with the CMB and EBL photons in the following way:

$$p + \gamma_{bg} = p + e^+ + e^- \qquad (4)$$

$$p + \gamma_{bg} \rightarrow \Delta^+ \rightarrow \begin{cases} n + \pi^+ \\ p + \pi^0. \end{cases} \qquad (5)$$

The neutral pions decay to gamma photons ($\pi^0 \rightarrow \gamma\gamma$) and the charged pions decay to neutrinos ($\pi^+ \rightarrow \mu^+ + \nu_\mu \rightarrow e^+ + \nu_e + \bar\nu_\mu + \nu_\mu$). The resulting cosmogenic neutrinos propagate

undeflected by magnetic fields and unattenuated by interaction with other particles.

The secondary $e^\pm$ and γ-rays initiate an electromagnetic (EM) cascade by undergoing pair production, inverse Compton upscattering of the background photons, and synchrotron radiation in the extragalactic magnetic field (EGMF). The resulting spectrum extends down to GeV energies and depends more on the propagation distance and background photon model than the injection parameters. We use the semianalytical EBL model given in Gilmore et al. (2012) for the propagation of UHECRs and the attenuation of secondary EM particles, and also the primary γ-rays coming from leptonic emission inside the source. UHECRs also interact with the universal radio background (Protheroe & Biermann 1996), which is important at energies higher than the Greisen–Zatsepin–Kuzmin (GZK) cutoff energy for Δ-resonance with the CMB photons. The EGMF causes a spreading of the UHECR beam and also the EM particles. We consider the contribution from the line-of-sight resolved component of the cascade spectrum to the observed SED (see Section 5).

We have used the publicly available simulation framework, CRPROPA 3 (Alves Batista et al. 2016, 2022; Heiter et al. 2018) to propagate UHECR protons from their source to the observer. The secondary EM particles are propagated in the CRProPa simulation chain, using a value of EM thinning $\eta = 0.6$.

4.3. pp Interactions

An alternative scenario is when the relativistic protons have much lower energy than UHECRs and they interact with the cold protons within the emission region as they are trapped in the magnetic field of the emission region. The proton–proton interactions result in the production of neutral and charged pions. These pions decay into secondary particles, e.g., electrons/positrons, neutrinos, and γ-rays. The proton–proton

Table 1
Results of Multiwavelength SED Modeling Shown in Figures 2, 3, and 4

Parameters	Pure Leptonic Model	Leptonic + Hadronic (UHECR) Model	Leptonic + Hadronic (pp) Model
Spectral index of injected electron spectrum (α)	2.2	2.2	2.2
Curvature index of injected electron spectrum (β)	0.06	0.06	0.10
Magnetic field in emission region (B)	0.10 G	0.10 G	0.10 G
Size of the emission region (R)	8.0×10^{15} cm	8.0×10^{15} cm	1.8×10^{16} cm
Doppler factor ($\delta_{\rm D}$)	20	20	20
Min. Lorentz factor ($\gamma_{\rm min}$)	1.0×10^{2}	1.0×10^{2}	2.5×10^{2}
Max. Lorentz factor ($\gamma_{\rm max}$)	9.0×10^{7}	9.0×10^{7}	9.0×10^{7}
Spectral index of relativistic proton spectrum (α_p)	...	2.2	2.2
Min. energy of relativistic protons ($E_{\rm p,min}$)	...	0.1 EeV	10 GeV
Max. energy of relativistic protons ($E_{\rm p,max}$)	...	100 EeV	10^4 GeV
Jet power of relativistic leptons (P_e)	2.6×10^{43} erg s^{-1}	2.6×10^{43} erg s^{-1}	2.2×10^{43} erg s^{-1}
Jet power of magnetic field (P_B)	9.6×10^{41} erg s^{-1}	9.6×10^{41} erg s^{-1}	4.9×10^{42} erg s^{-1}
Jet power of relativistic protons (P_p)	...	1.9×10^{42} erg s^{-1}	9.8×10^{44} erg s^{-1}
Kinematic jet power ($P_{\rm tot}^k$)	2.7×10^{43} erg s^{-1}	2.9×10^{43} erg s^{-1}	1.0×10^{45} erg s^{-1}

interaction channels can be shown in the following manner:

$$p + p \rightarrow \begin{cases} \pi^\circ \rightarrow \gamma + \gamma \\ \pi^+ \rightarrow \nu_\mu + \mu^+ \rightarrow \nu_\mu + e^+ + \nu_e + \bar{\nu}_\mu \\ \pi^- \rightarrow \bar{\nu}_\mu + \mu^- \rightarrow \bar{\nu}_\mu + e^- + \bar{\nu}_e + \nu_\mu. \end{cases} \quad (6)$$

We have considered a power-law proton injection spectrum within the emission region, with a spectral index α_p and minimum $E_{\rm p,min}$ and maximum energy $E_{\rm p,max}$. We have used the publicly available code GAMERA for the time-independent pp modeling. It uses the formalism given in Kafexhiu et al. (2014). There are four hadronic interaction models that are included in this code, and for our work, we have used the one given by PYTHIA 8.18 (Sjöstrand et al. 2008).

We have balanced the total charge in the emission region to determine the total number of protons. The γ-ray spectrum produced in pp interactions has been corrected for internal absorption by the lower-energy photons inside the blob, and also for absorption by the EBL.

4.4. Jet Power

We have calculated the kinematic jet power using the following equation:

$$P_{\rm tot}^k = P_e + P_B + P_p = \pi R^2 \Gamma^2 c(u'_e + u'_p + u'_B), \quad (7)$$

where $P_{\rm tot}^k$ is the kinematic jet power and Γ is the bulk Lorentz factor; u'_e, u'_p, and u'_B are the energy densities of the relativistic electrons (and positrons), protons, and magnetic field respectively in the comoving jet frame (Banik & Bhadra 2019; Banik et al. 2020). The primed and unprimed notations denote quantities in the comoving jet frame and the AGN frame, respectively. We have maintained the charge neutrality condition in the jet. If we add the jet power of cold protons the luminosity budget in the proton–proton interaction model exceeds the Eddington luminosity as discussed in Banik & Bhadra (2019) and Banik et al. (2020). A sub-Eddington jet power in the proton–proton interaction model is possible in the scenario discussed in a recent paper (Xue et al. 2022) after including the jet power in cold protons. However, we compare only the kinematic jet power to the Eddington luminosity, as has been done in earlier papers.

Here, we have considered that the bulk Lorentz factor (Γ) and Doppler factor ($\delta_{\rm D}$) are equal. We have presented the jet powers of individual components and the total kinematic jet power in Table 1.

The mass of the black hole of Mrk 180 as reported in earlier papers has been used to calculate the Eddington luminosity. According to Treves et al. (2003) the value of $\log_{10}(M_{\rm BH}/M_\odot)$ is 8.59, and according to Falomo et al. (2003) it is 8.70, where $M_{\rm BH}$ is the mass of the black hole and $M_\odot$ is the solar mass. Using these values, we have calculated the Eddington luminosity ($L_{\rm Edd}$) of Mrk 180, which is 5.06×10^{46} erg s^{-1} and 6.51×10^{46} erg s^{-1} respectively. The total kinematic jet powers obtained in our models are less than the Eddington luminosity of Mrk 180.

5. Results

Mrk 180/Mkn 180/TeV J1136+701 or 4FGL J1136.4 +7009 is an HBL-type blazar at a redshift of 0.045. This source is monitored by several telescopes, viz. Fermi-LAT, Swift, XMM-Newton, MOJAVE, MAGIC, KVA, ASM, RATAN-600, Metsähovi, Effelsberg, and Institute for Radio Astronomy in the Millimeter range (IRAM) throughout the year, and it was closely monitored during the high state in the optical wave band in 2006.

12.8 yr (MJD 54,682.65–59,335.67) of Fermi-LAT γ-ray data of Mrk 180 has been analyzed in this work. Besides Fermi-LAT γ-ray data, we also collected data in other wave bands, e.g., Swift, XMM-Newton, MOJAVE, and MAGIC. Figure 1 is the long-term Fermi-LAT γ-ray light curve in 30 day binning. As can be seen from Section 3, this long-term light curve does not show any significant flaring throughout this time; also the error bars of the high-energy γ-ray data points are large, hence a more detailed analysis of the light curve cannot give us any useful information. To know about the physical processes that can explain the observed spectrum, we studied the long-term SED of Mrk 180, where we used multiwavelength data from different telescopes. The multi-wavelength SED shows the double hump structure, which has been modeled with GAMERA, considering a simple one-zone spherical emission region within the jet. In Figures 2, 3, and 4, we have shown the multiwavelength SEDs fitted with different models, e.g., pure leptonic and lepto-hadronic. Also, we have
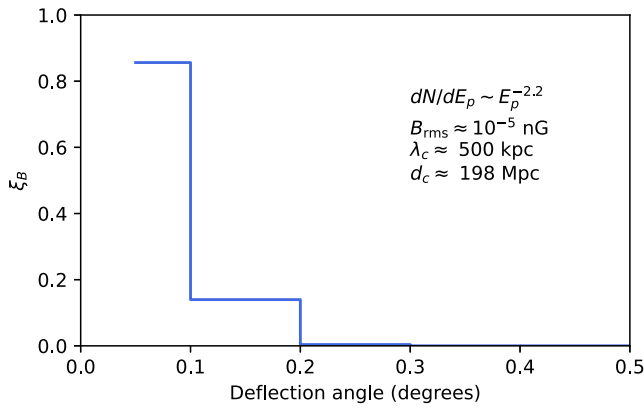
Figure 5. Distribution of propagated UHECRs as a function of deflection angle in a random turbulent magnetic field.

shown the residual (data – model/error) plot corresponding to the fit to each model in Figures 2, 3, and 4.

First, we consider a pure leptonic model (Figure 2), where the first hump is produced by the synchrotron radiation of the relativistic electrons, and the second hump is produced by upscattering of the synchrotron photons by the relativistic electrons. As discussed in Section 4.1, we consider a spherical emission region or blob of radius R within the blazar jet. Leptons are injected within the blob following an injection spectrum (Equation (1)). The best-fitted parameter values corresponding to this modeling, e.g., spectral index (α) and curvature index (β), are listed in the first column of Table 1. We have mentioned the jet power of different components, e.g., relativistic leptons (P_e), magnetic field (P_B), and relativistic protons (P_p), in Table 1, and also the total kinematic jet power (P_{tot}^k), which is the sum of the jet power of all the components of a model.

The pure leptonic model is found to be insufficient to explain the multiwavelength SED, as the highest-energy γ-ray data point cannot be fitted with this model. Moreover, the slope of the observed X-ray spectrum does not match the slope of the synchrotron spectrum obtained in our model. To improve the fit to the multiwavelength SED, particularly in the VHE γ-ray regime, we check the fit with lepto-hadronic models. As discussed earlier, we have considered two kinds of hadronic processes, viz., the interaction of UHECRs with the background photons and the pp interaction within the blob.

In the case of UHECRs (for simplicity we consider only protons), the escape of protons from the blazar jet can dominate over the energy loss inside the blazar jet. We consider a power-law injection of protons into the ISM following Equation (3). We have considered proton injection into the ISM between $E_{p,\text{min}} = 0.1$ EeV and $E_{p,\text{max}} = 100$ EeV. The injection spectral index $\alpha_p = 2.2$ is the same as for leptons. In the UHECR interaction model, we consider the three-dimensional propagation of UHECRs to calculate the fraction of them that survive within $0°.1$ of the initial emission direction and denote it by ξ_B. Protons are propagated from the source at a comoving distance of $\sim$200 Mpc and collected over a spherical region of radius 1 Mpc. We consider a random turbulent EGMF given by a Kolmogorov power spectrum, an rms field strength of $B_{\text{rms}} \approx 10^{-5}$ nG, and a coherence length of 0.5 Mpc using wave modes between 80 kpc and 2.25 Mpc. The distribution of the survival fraction with deflection angle is shown in Figure 5. We multiply the flux of the cosmogenic γ-ray spectrum by ξ_B to take into account the γ-rays reaching the observer from the

direction of the blazar. The Fermi-LAT resolution to a single photon above 10 GeV is $\sim$0°.15.

Figure 3 is the resulting fit corresponding to this model. The green curve indicates the spectrum of cosmogenic photons. The required power in UHECR protons is calculated in the following manner (Das et al. 2020):

$$P_{\text{UHECR}} = \frac{2\pi d_L^2 (1 - \cos\theta_{\text{jet}})}{\xi_B f_{\text{CR}}} \int_{\epsilon_{\gamma,\text{min}}}^{\epsilon_{\gamma,\text{max}}} \epsilon_\gamma \frac{dN}{d\epsilon_\gamma dA dt} d\epsilon_\gamma \quad (8)$$

where d_L is the luminosity distance of Mrk 180, θ_{jet} is the jet opening angle, and ξ_B is the survival rate of UHECRs within $0°.1$ of the direction of propagation to the observer. The quantity f_{CR} is the fraction of UHECR luminosity that goes into cosmogenic γ-rays and depends on the propagation distance. The integration is done over the cosmogenic photon spectrum allowed by the observed SED. d_L is 207 Mpc, θ_{jet} is 0.1 rad (we have considered a typical value of θ_{jet}) (Pushkarev et al. 2009; Finke 2019), and $\Gamma = 20$. For the chosen parameters, $\xi_B = 0.85$ and $f_{\text{CR}} = 0.03$. Putting these values into Equation (8), P_{UHECR} has been calculated. Finally, we add up the total kinematic jet power of the relativistic leptons, magnetic field, and UHECRs denoted by P_{UHECR} to get the total kinematic jet power for this model to be 2.9×10^{43} erg s^{-1}, which is less than the Eddington luminosity of Mrk 180 by several orders of magnitude. The best-fitted values of this model are tabulated in the second column of Table 1. In this case, the highest-energy MAGIC data point can be fitted, but the fit to the X-ray data points has not improved.

We subsequently consider the pp interactions within the jet. As explained in Section 4.3, the relativistically accelerated protons interact with cold protons and produced neutral and charged pions, which decay into photons, leptons, and neutrinos. A power-law proton spectrum is injected within the blob with a spectral index $\alpha_p = 2.2$, minimum energy ($E_{p,\text{min}}$) 10 GeV, and maximum energy ($E_{p,\text{max}}$) 10^4 GeV, and the cold proton density is assumed to be $n_H = 1.2 \times 10^6$ cm^{-3}. These parameter values have been presented in the third column of Table 1. Previously, Banik & Bhadra (2019) showed that the pp interaction model can explain the observed high-energy γ-rays from the blazar TXS 0506+056 for $n_H = 1.68 \times 10^6$ cm^{-3}. Aharonian (2000) showed that high-energy γ-ray production in an AGN jet via pp interaction demands a high cold proton density, and that to interpret the reported TeV flares of Markarian 501 by pp interactions, n_H should exceed 10^6 cm^{-3}.

From Figure 2 we can see that the SED from the pure leptonic model cannot fit the Swift UV data points. The slope of the observed X-ray and γ-ray data points cannot be explained with the slope of the theoretical SED; also it poorly fits the γ-ray data points. The residual plot corresponding to the pure leptonic model shows that this model poorly fits the Swift UV data, X-ray data, and MAGIC data.

From Figure 3 it can be seen that UHECR interactions make the fit better for the MAGIC data points but the slope of the SED from this model does not match the slope of the X-ray data. Moreover, the Swift UV data cannot be fitted well with this model. The residual plot corresponding to this model looks almost the same as that for the pure leptonic model between 10^{-5} and 10^{11} eV, except for the MAGIC data points.
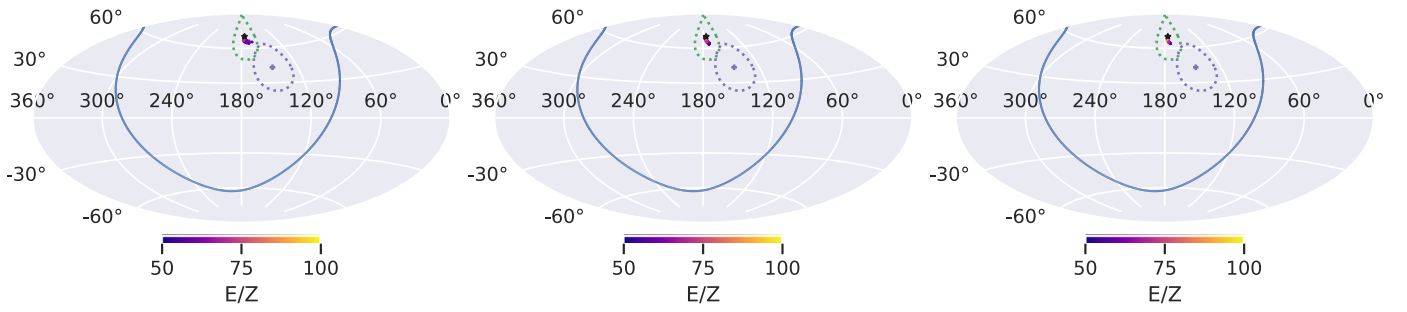
Figure 6. Arrival direction of UHECRs at $E > 57$ EeV from Mrk 180 to Earth. The blue line shows the Galactic plane. The purple point and the purple dotted curve show the center of the TA hotspot and the $20°$ region around it. Similarly, the green dotted curve shows the $20°$ region around Mrk 180. The color bar indicates the energy per nucleon (E/z) of the observed events. From left, the figures correspond to (a) pure proton injection and $B_{\rm rms} \approx 10^{-3}$ nG, (b) pure proton injection and $B_{\rm rms} \approx 10^{-5}$ nG, and (c) Fe injection and $B_{\rm rms} \approx 10^{-5}$ nG.

Figure 4 shows improvement in both SED and the residuals. The SED fits the Swift UV data points and matches the slope of the X-ray data and the γ-ray data. The residual plot corresponding to this model shows that the residuals for the Swift UV data points lie between $\sim\pm10$, whereas they lie between $+10$ and $+20$ in Figures 2 and 3. In Figure 4, the residuals for the Swift XRT and XMM-Newton EPIC-MOS data lie within ±10 and the XMM-Newton EPIC-pn data lie beyond $+10$. In the previous two plots, i.e., Figures 2 and 3, all the residuals for the X-ray data points lie within $+10$ to -20. It is clear from the residual plot that the SED is not very well fitted, which is why we are getting large values of the residuals. We have not shown the residuals for the Swift optical data points, as they cannot be fitted with any of these models. Most of the γ-ray data points can be fitted in this model. The total kinematic jet power corresponding to each model is less than the Eddington luminosity of Mrk 180, which is mentioned in Table 1.

5.1. UHECRs from Mrk 180

It has been proposed previously (He et al. 2016) that Mrk 180 may be a source contributing to the UHECR hotspot observed by the TA collaboration above 57 EeV. We propagate UHECRs from the source to the Earth in a random turbulent magnetic field given by the Kolmogorov power spectrum. We consider three different combinations of the rms value of the EGMF ($B_{\rm rms}$) and composition at the source as shown in Figure 6. The turbulence correlation length of the EGMF is taken to be 0.5 Mpc. The Galactic magnetic field (GMF) model is considered to be the one given in Jansson & Farrar (2012). We inject cosmic rays with a generic power-law spectrum given by $dN/dE \sim E^{-2}$ and perform three-dimensional simulations including both GMF and EGMF in CRPROPA 3 (Alves Batista et al. 2016, 2022). We consider two cases of composition with extreme masses, viz., ^{1}H and ^{56}Fe. For pure proton injection, the magnetic rigidity is higher and the resulting deflection is low.

We show the case of $B_{\rm rms} \sim 10^{-3}$ nG and 10^{-5} nG in the left and middle panels of Figure 6 for proton injection. For the same injected luminosity, the number of detected events in the former case is 35, while that for the latter increases by almost three orders of magnitude. It can be seen that even with Fe injection (see right panel in Figure 6), the angular width of the source observed through UHECRs does not show a significant change, although the observed energy spectrum is different. Due to the photodisintegration of the nuclei traversing a comoving distance of $\sim$200 Mpc, the observed events at Earth

for the energy range considered are all protons. Thus, it can be seen that for optimistic magnetic field values considered, the contribution of this source to the TA hotspot is disfavored unless very high magnetic fields $\mathcal{O} \sim 1$ nG or higher are considered. Although a greater spread in the arrival direction is expected if the detection threshold is lowered, the Galactic magnetic field shadows the directional signatures. Thus, Mrk 180 may not be a plausible UHECR source for explaining the TA hotspot.

6. Discussions

Being at a redshift of 0.045, Mrk 180 is an interesting source to study the radiative mechanisms producing TeV γ-rays. VHE γ-ray emission from this source was detected by MAGIC in 2006 (Albert et al. 2006) followed by an enhanced optical state. This source has been monitored by several telescopes throughout the year, as mentioned in Section 5. Previously, Rügamer et al. (2011a, 2011b) studied this source using multiwavelength data. They discussed the results of the multiwavelength campaign in 2008 that covered radio to TeV γ-ray observations. At that time Mrk 180 was known to be a TeV γ-ray source detected by MAGIC only a couple of years previously. Their study reported the first multiwavelength campaign on Mrk 180. Optical observation was carried out by the KVA telescope simultaneously with TeV γ-ray observation with MAGIC. The radio observation was carried out with RATAN-600, Metsähovi, Effelsberg, and IRAM. Swift XRT detected flux variability in X-rays. In the same observation window of Swift XRT, Metsähovi and AGILE could not detect this source. The Fermi-LAT light curve showed enhancement in γ-ray flux during the second flare.

Rügamer et al. tried to explain the simultaneous multiwavelength SED of Mrk 180 by two models: (1) a one-zone SSC model and (2) a self-consistent two-zone SSC model; they considered the injected electron spectrum as a broken power-law distribution. It can be seen in Rügamer et al. (2011a) that during the high state neither model can explain the multiwavelength data properly. The steep X-ray spectrum and high optical flux could not be explained simultaneously assuming they were produced in the same zone. Moreover, in the two-zone SSC model the required value of the Doppler factor $\delta_{\rm D}$ is very high. During the low X-ray state both the models can explain the SED for moderate values of parameters. Nilsson et al. (2018) studied R-band long-term optical data (over a span of $\sim$10 yr) of 31 northern blazars including Mrk 180. They could not find any significant periodicity for this source. The earlier multiwavelength studies on Mrk 180 have been

complemented in this work with more data analysis and theoretical modeling of the SED over a long period of observations.

For the temporal study, we analyzed 12.8 yr (MJD 54,682.65–59,355.67) of Fermi-LAT γ-ray data. Figure 1 is the long-term Fermi-LAT γ-ray light curve in 30 day binning. No γ-ray flux enhancement has been found from this long-term light curve; also the error bars of the high-energy γ-ray data points are too large to carry out a detailed temporal study on this source. To know about the physical processes we studied the long-term SED of Mrk 180. For this study, we have used multiwavelength data from MOJAVE, MAGIC, Swift, XMM-Newton, and Fermi-LAT. The SED shows typically the double hump structure. We have modeled this multiwavelength SED with GAMERA. We have considered a simple one-zone spherical emission region within the jet. In Figures 2, 3, and 4, we have shown the modeled multiwavelength SEDs with different models, e.g., pure leptonic and lepto-hadronic. Also, we have shown the residual plots of each model, attached just below that particular SED. The results of the multiwavelength SED modeling with different models have already been discussed in Section 5. The leptonic modeling is not sufficient to explain the multiwavelength SED of Mrk 180. We have considered two lepto-hadronic models to improve the fit to the observed data points. The first model involves interactions of UHECRs injected by Mrk 180 with the radiation backgrounds, and in the second model we have considered interactions of relativistic protons in the jet with cold protons. The latter gives a slightly better fit to the data; however, more observational data are necessary to explain the radiation mechanisms in Mrk 180, because our results show large values of residuals in all the cases. We look forward to future multiwavelength campaigns to cover all the frequencies over a long time period to monitor this source more closely.

He et al. (2016) calculated the probability associated with some sources being contributors to the TA hotspot, Mrk 180 is one of them. It is important to know the role of Mrk 180 as a UHECR accelerator, and whether it can generate events above 57 EeV. In our study for conservative values of EGMF, Mrk 180 is disfavoured as a source of the UHECR events contributing to the TA hotspot. In future, with more observational data it would be interesting to study the association of Mrk 180 with the TA hotspot.

7. Conclusion

The HBL Mrk 180, at a redshift of 0.045, is an interesting source to study the emission covering radio to VHE γ-ray frequencies. We have analyzed the Fermi-LAT γ-ray data detected from this source over a period of 12.8 yr. The light curve analysis does not show any significant variation in flux. We have studied the long-term multiwavelength SED of this source to understand the physical processes that can explain the HBL nature of this source. We modeled the multiwavelength SED with a time-dependent code "GAMERA." It is found that a single-zone pure leptonic model cannot explain the multi-wavelength spectrum of Mrk 180 properly. We considered single-zone lepto-hadronic models to obtain better fits to the data. The residuals of the three models are compared and the pp interaction model is found to give a better fit to the multiwavelength data than the other two models. More observational data covering the radio to VHE γ-ray frequencies would be useful for exploring the emission mechanisms of Mrk

180 and to give a definitive conclusion. The possible association of Mrk 180 with the TA hotspot events above 57 EeV has also been examined using the simulation framework CRPROPA 3 (Alves Batista et al. 2016, 2022). In this study we do not find any UHECR event from Mrk 180 contributing to the TA hotspot, hence we conclude that for conservative values of EGMF, Mrk 180 is disfavoured as a source contributing to the TA hotspot; however, in future with more UHECR data it would be possible to investigate their association further.

8. Software and Third-party Data Repository Citations

The Fermi-LAT γ-ray data analysis was done with "Fermipy" (Wood et al. 2017). Swift X-ray, ultraviolet, and optical data have been analyzed with "HEASoft" (NASA High Energy Astrophysics Science Archive Research Center (Heasarc) 2014). To analyze XMM-Newton data, we have used Science Analysis System (SAS, Gabriel et al. 2004).

Facilities: Swift(XRT and UVOT), XMM-Newton, Fermi-LAT, MAGIC.

Software: Fermipy (https://fermipy.readthedocs.io/en/latest/; Wood et al. 2017), HEASoft (https://heasarc.gsfc.nasa.gov/docs/software/lheasoft/; Nasa High Energy Astrophysics Science Archive Research Center (Heasarc) 2014), SAS (https://www.cosmos.esa.int/web/xmm-newton/sas-threads; Gabriel et al. 2004), GAMERA (http://libgamera.github.io/GAMERA/docs/main_page.html; Hahn 2016), CRPropa 3 (https://crpropa.github.io/CRPropa3/; Alves Batista et al. 2016, 2022).

ORCID iDs

Sandeep Kumar Mondal ⬤ https://orcid.org/0000-0003-2445-9935
Saikat Das ⬤ https://orcid.org/0000-0001-5796-225X
Nayantara Gupta ⬤ https://orcid.org/0000-0002-1188-7503

References

Abbasi, R. U., Abe, M., Abu-Zayyad, T., et al. 2014, ApJL, 790, L21
Acero, F., Ackermann, M., Ajello, M., et al. 2016, ApJS, 223, 26
Aharonian, F. 2000, NewA, 5, 377
Albert, J., Aliu, E., Anderhub, H., et al. 2006, ApJ, 648, L105
Alves Batista, R., Dundovic, A., Erdmann, M., et al. 2016, JCAP, 2016, 038
Alves Batista, R., Becker Tjus, J., Dörner, J., et al. 2022, JCAP, 2022, 035
Arnaud, K. A. 1996, in ASP Conf. Ser. 101, Astronomical Data Analysis Software and Systems V, ed. G. H. Jacoby & J. Barnes (San Francisco, CA: ASP), 17
Atwood, W. B., Abdo, A. A., Ackermann, M., et al. 2009, ApJ, 697, 1071
Ballet, J., Burnett, T. H., Digel, S. W., & Lott, B. 2020, arXiv:2005.11208
Banik, P., & Bhadra, A. 2019, PhRvD, 99, 103006
Banik, P., Bhadra, A., Pandey, M., & Majumdar, D. 2020, PhRvD, 101, 063024
Blandford, R., Meier, D., & Readhead, A. 2019, ARA&A, 57, 467
Bruel, P., Burnett, T. H., Digel, S. W., et al. 2018, arXiv:1810.11394
Burrows, D. N., Hill, J. E., Nousek, J. A., et al. 2005, SSRv, 120, 165
Cerruti, M. 2020, Galax, 8, 72
Das, S., Gupta, N., & Razzaque, S. 2020, ApJ, 889, 149
Doro, M., Bastieri, D., Biland, A., et al. 2008, NIMPA, 595, 200
Essey, W., Kalashev, O. E., Kusenko, A., & Beacom, J. F. 2010, PhRvL, 104, 141102
Essey, W., & Kusenko, A. 2010, APh, 33, 81
Extinction 2016, Extinction, https://extinction.readthedocs.io/en/latest/#

Falomo, R., Kotilainen, J., & Treves, A. 2003, in The Mass of Galaxies at Low and High Redshift, Proc. European Southern Observatory and Universitäts-Sternwarte München Workshop, ed. R. Bender & A. Renzini (Berlin: Springer), 109

Fermi-LAT Data Server 2022, Fermi-LAT Collaboration, https://fermi.gsfc.nasa.gov/cgi-bin/ssc/LAT/LATDataQuery.cgi

Fermi-LAT Ciceron 2022, https://fermipy.readthedocs.io/en/latest/

Fermipy Document 2022, Fermipy, https://fermipy.readthedocs.io/en/latest/

Finke, J. D. 2019, ApJ, 870, 28

Fitzpatrick, E. L. 1999, PASP, 111, 63

Gabriel, C., Denby, M., Fyfe, D. J., et al. 2004, in ASP Conf. Ser, 314, Astronomical Data Analysis Software and Systems (ADASS) XIII, ed. F. Ochsenbein, M. G. Allen, & D. Egret (San Francisco, CA: ASP), 759

GAMERA 2016, GAMERA, https://github.com/libgamera/GAMERA

Gilmore, R. C., Somerville, R. S., Primack, J. R., & Dominguez, A. 2012, MNRAS, 422, 3189

Hahn, J. 2016, ICRC (The Hague), 34, 917

He, H.-N., Kusenko, A., Nagataki, S., et al. 2016, PhRvD, 93, 043011

Heiter, C., Kuempel, D., Walz, D., & Erdmann, M. 2018, APh, 102, 39

HI4PI Collaboration, Ben Bekhti, N., Flöer, L., et al. 2016, A&A, 594, A116

Hutter, D. J., & Mufson, S. L. 1981, AJ, 86, 1585

Jansson, R., & Farrar, G. R. 2012, ApJ, 757, 14

Kafexhiu, E., Aharonian, F., Taylor, A. M., & Vila, G. S. 2014, PhRvD, 90, 123014

Kawata, K., di Matteo, A., Fujii, T., et al. 2019, ICRC, 36, 310

Kawata, K., Fukushima, M., Ikeda, D., et al. 2015, ICRC (The Hague), 34, 276

Lister, M. L., Aller, M. F., Aller, H. D., et al. 2018, ApJS, 234, 12

MAGIC Data Centre 2006, MAGIC, http://vobs.magic.pic.es/fits/#database

Massaro, E., Perri, M., Giommi, P., & Nesci, R. 2004, A&A, 413, 489

MOJAVE_Source_Page 2016, MOJAVE Source Page, https://www.cv.nrao.edu/MOJAVE/sourcepages/1133+704.shtml

MOJAVE Webpage 2016, MOJAVE Webpage, https://www.cv.nrao.edu/MOJAVE/index.html

Mufson, S. L., & Hutter, D. J. 1981, ApJL, 248, L61

Nasa High Energy Astrophysics Science Archive Research Center (Heasarc) 2014, HEAsoft: Unified Release of FTOOLS and XANADU, Astrophysics Source Code Library, ascl:1408.004

Nilsson, K., Lindfors, E., Takalo, L. O., et al. 2018, A&A, 620, A185

om2pha 2016, om2pha, https://www.cosmos.esa.int/web/xmm-newton/sas-thread-om2pha

omichain 2018, omichain, https://www.cosmos.esa.int/web/xmm-newton/sas-thread-omi

OMResponseFile 2008, OMResponseFile, esac.esa.int/pub/ccf/constituents/extras/responses/OM/

Protheroe, R. J., & Biermann, P. L. 1996, APh, 6, 45

Pushkarev, A. B., Kovalev, Y. Y., Lister, M. L., & Savolainen, T. 2009, A&A, 507, L33

Rieke, G. H., & Lebofsky, M. J. 1985, ApJ, 288, 618

Rügamer, S., Angelakis, E., Bastieri, D., et al. 2011a, arXiv:1110.6341

Rüamer, S., Angelakis, E., Bastieri, D., et al. 2011b, arXiv:1109.6808

Scargle, J. D., Norris, J. P., Jackson, B., & Chiang, J. 2013, arXiv:1304.2818

Schultz, G. V., & Wiemer, W. 1975, A&A, 43, 133

Sjöstrand, T., Mrenna, S., & Skands, P. 2008, CoPhC, 178, 852

SSDC, I. S. A. 2000, SSDC, https://tools.ssdc.asi.it/SED/

Tchernin, C., Aguilar, J. A., Neronov, A., & Montaruli, T. 2014, NIMPA, 742, 191

Treves, A., Carangelo, N., Falomo, R., & Kotilainen, J. 2003, in ASP Conf. Ser. 290, Active Galactic Nuclei: From Central Engine to Host Galaxy, ed. S. Collin, F. Combes, & I. Shlosman (San Francisco, CA: ASP), 621

Ulrich, M.-H. 1978, ApJ, 222, L3

Urry, C. M., & Padovani, P. 1995, PASP, 107, 803

Whittet, D. C. B., & van Breda, I. G. 1980, MNRAS, 192, 467

Wood, M., Caputo, R., Charles, E., et al. 2017, ICRC, 35, 824

Xue, R., Wang, Z.-R., & Li, W.-J. 2022, PhRvD, 106, 103021